Observation of multi-directional energy transfer in a hybrid plasmonic-excitonic nanostructure

Tommaso Pincelli † Thomas Vasileiadis † Shuo Dong Samuel Beaulieu Maciej Dendzik Daniela Zahn Sang-Eun Lee Hélène Seiler Yinpeng Qi R.Patrick Xian Julian Maklar Emerson Coy Niclas S. Müller Yu Okamura Stephanie Reich Martin Wolf Laurenz Rettig Ralph Ernstorfer**

† These authors contributed equally.

Dr. T. Pincelli, Dr. T. Vasileiadis, Dr. S. Dong, Dr. S. Beaulieu, Dr. M. Dendzik, Dr. D. Zahn, S.-E. Lee, Prof. H. Seiler, Dr. Y. Qi, Dr. R. P. Xian, J. Maklar, Prof. M. Wolf, Dr. L. Rettig, Prof. Ernstorfer
Fritz-Haber-Institut der Max-Planck-Gesellschaft, Faradayweg 4-6, 14195 Berlin, Germany
Email Address: pincelli@fhi-berlin.mpg.de, ernstorfer@fhi-berlin.mpg.de
Prof. H. Seiler, Dr. N. S. Mueller, Y. Okamura, Prof. S. Reich
Freie Universität Berlin, Arnimallee 14, 14195 Berlin, Germany.
Dr. T. Pincelli, Prof. R. Ernstorfer
Institut für Optik und Atomare Physik, Technische Universität Berlin, Straße des 17. Juni 135, 10623 Berlin, Germany
Dr. T. Vasileiadis
Faculty of Physics, Adam Mickiewicz University, Uniwersytetu Poznanskiego 2, 61-614 Poznan, Poland
Dr. S. Beaulieu
Université de Bordeaux - CNRS - CEA, CELIA, UMR5107, F33405, Talence, France.
Dr. M. Dendzik
Department of Applied Physics, KTH Royal Institute of Technology, Hannes Alfvéns väg 12, 114 19 Stockholm, Sweden.
Dr. Y. Qi
Center for Ultrafast Science and Technology, School of Physics and Astronomy, Jiao Tong University, 200240 Shanghai, China.
Dr. R. P. Xian
Department of Statistical Sciences, University of Toronto, 700 University Avenue, Toronto, M5G 1Z5, Canada.
Dr. E. Coy
NanoBioMedical Centre, Adam Mickiewicz University, ul. Wszechnicy Piastowskiej 3, PL 61614 Poznań, Poland.
Dr. N. S. Mueller
NanoPhotonics Centre, Kapitza Building, Cavendish Laboratory, J. J. Thomson Avenue, Cambridge CB3 0HE, UK.

Keywords: *hybrid plasmonics, time resolved ARPES, femtosecond electron diffraction, interfacial charge transfer, 2D semiconductors.*

Abstract: Hybrid plasmonic devices involve a nanostructured metal supporting localized surface plasmons to amplify light-matter interaction, and a non-plasmonic material to functionalize charge excitations. Application-relevant epitaxial heterostructures, however, give rise to ballistic ultrafast dynamics that challenge the conventional semi-classical understanding of unidirectional nanometal-to-substrate energy transfer. We study epitaxial Au nanoislands on WSe_2 with time-, angle-resolved photoemission spectroscopy and femtosecond electron diffraction: this combination resolves material, energy and momentum of charge-carriers and phonons. We observe a strong non-linear plasmon-exciton interaction that transfers the energy of sub-bandgap photons very efficiently to the semiconductor, leaving the metal cold until non-radiative exciton recombination heats the nanoparticles after 200 fs. Our results resolve a multi-directional energy exchange on timescales shorter than the electronic thermalization of the nanometal. Electron-phonon coupling and diffusive charge-transfer determine the subsequent energy flow. This complex dynamics opens perspectives for optoelectronic and phtocatalitic applications, while providing a constraining experimental testbed for state-of-the-art modelling.

1 Introduction

Irradiation of nanometals with light drives collective oscillations of charge-carriers (plasmons) and light localization beyond the diffraction limit in plasmonic near-fields. The energy of plasmons dissipates within tens of femtoseconds, either radiatively by photon emission, or in electron-hole excitations, producing non-equilibrium carrier distributions.

In recent years, the focus of plasmonics is oriented towards plasmonic energy harvesting [1, 2, 3]. The nascent field of hybrid plasmonics seeks to interface metal nanostructures with other materials, and in particular semiconductors, which convert plasmons to electronic excitations with impactful applications. Hybrid plasmonics devices are useful in light-harvesting, photochemistry, photocatalysis, photodetectors and single-molecule detectors [4, 5, 2, 6, 7]. For these applications, radiative losses are suppressed, e.g., by minimizing the metallic nanoparticles' volume [8], while hot-carrier injection is maximized by creating a strong exciton-plasmon interaction. This is achieved when the plasmonic hot carriers ejection is more efficient than internal thermalization by electron-phonon coupling.

The challenges in the microscopic description of hybrid plasmonic systems stem from the strong inhomogeneity of the hot-carrier distributions both in real space and, for the case of crystals with well-defined Bloch states, also in reciprocal space. In these conditions, the assumptions of homogeneous hot carrier generation and instant thermalization (that proved effective for larger nanoparticles in colloidal suspensions) are no longer applicable: geometry-assisted intraband transitions dominate plasmon decoherence dynamics enhancing the hot carrier distribution at the surface [9, 10], narrow gaps between the nanoparticles generate regions of enhanced polarization of the substrate [11], and unoccupied states in the semiconductor offer high-energy excitation transitions across the interface at selected momentum matched locations [12, 13]. Furthermore, the coupling of the electronic system with phononic excitations, and the subsequent energy flow leading back to thermodynamic equilibrium, are critical in determining the subsequent functionalities achievable by devices based on the hybrid interface [14].

We focus on achieving a fundamental understanding of how strong interaction influences the interfacial energy flow in a rapidly emerging class of heterostructures formed by noble metals interfaced with transition metal dichalcogenides. The 2D van der Waals crystals, with their long lived and strongly bound excitons, promise a unique playground for hybrid plasmonics, and have been proven to exhibit strong exciton-plasmon coupling up to room temperature[15, 16]. The TMD-noble metal interface has been realized both in configurations where the TMD has a nanoscale structure [17, 18, 19] and in devices where the 3D metal is

laterally confined [20, 21, 22, 16, 23, 15]. Nano-TMD on extended Au do present fascinating possibilities for the control of surface plasmons owing to their large dielectric functions [18] and have enjoyed a significant effort devoted to understanding the microscopic mechanisms behind interfacial dynamics and band alignment [17, 24, 25, 19]. We focus, instead, on nano-structured Au on extended TMD, which has been recently employed to realize several devices with advanced plasmonic functionality [20, 23] or strong coupling [15, 21, 22, 16], but whose investigation of microscopic mechanisms has been less extensive.

Satisfactory modelling of microscopic charge-transfer mechanisms has been recently achieved with ab initio calculations that go beyond the simple jellium model [26, 13], but disentangling the same processes experimentally is challenging, as it requires monitoring several microscopic subsystems and their couplings at femtosecond timescales, as shown in Figure 1 a. The vast majority of experimental studies employed time-resolved optical spectroscopies [21, 22], with techniques that have limited access to optically dark excitations and to the details of quasiparticle scattering pathways in momentum space. We propose an approach that offers the opportunity to ground the study of plasmonic dynamics with an unprecedented detail of physical evidence, resolving the dynamics of the electronic states in momentum space and the coupling of charge excitations to phonons: this provides a direct response to the needs of hybrid plasmonics as foreseen by Linic et al.[3].

Here, we study a heterostructure of Au nanoislands on WSe_2 (Fig. 1 a) with time- and angle-resolved photoemission spectroscopy (tr-ARPES) that gives access to equilibrium and excited electronic states with momentum resolution [17, 27, 28] (Fig. 1 b), captures excitons in the TMD [29] and detects the dynamic hot-carrier distributions in the nanometal [30]. To fully unfold the dynamics of the system we investigate also the complementary subsystem, the lattice, by femtosecond electron diffraction (FED) [31, 32, 33](Fig. 1 c,f), determining the coupling of electronic excitations to phononic states.

Further support is provided by electronic structure calculations using density functional theory and finite elements calculations to investigate the distribution of interfacial fields. With this toolset we show that strong exciton-plasmon interactions can produce multi-directional of charge- and energy-flow between metal and semiconductor at extremely short timescales, a picture rather different from what is expected in traditional plasmonic approaches and semiclassical models both at the femtosecond and picosecond timescale. By determining the origins and timescales of such transient energy transfers, our results provide important insight for the design of a wide set of hybrid heterostructures that are object of very active investigation [34, 35, 36], as well as an accurate and constraining experimental test for the advanced theoretical models being developed for hybrid plasmonics.

2 Results

The Au nanoislands grow epitaxially on bulk WSe_2 with a random distribution of sizes and shapes, as displayed by TEM micrography in Fig. 1 d. The average lateral size is 10 nm with 2 nm average thickness (see SI Sect. 1). Optical absorption spectroscopy of bare and Au-decorated WSe_2 shows a significant modification of the absorbance (Fig. 1 e): a suppression of the WSe_2 A-exciton peak is accompanied by an increased absorption at $\lambda \geq 800$ nm which, as we will show, arises from localized, plasmon-assisted photoabsorption in the nanoparticle array. The stochastic distribution of sizes and shapes results in a broadly varying enhancement of the absorption within the bandgap of the semiconductor, rather

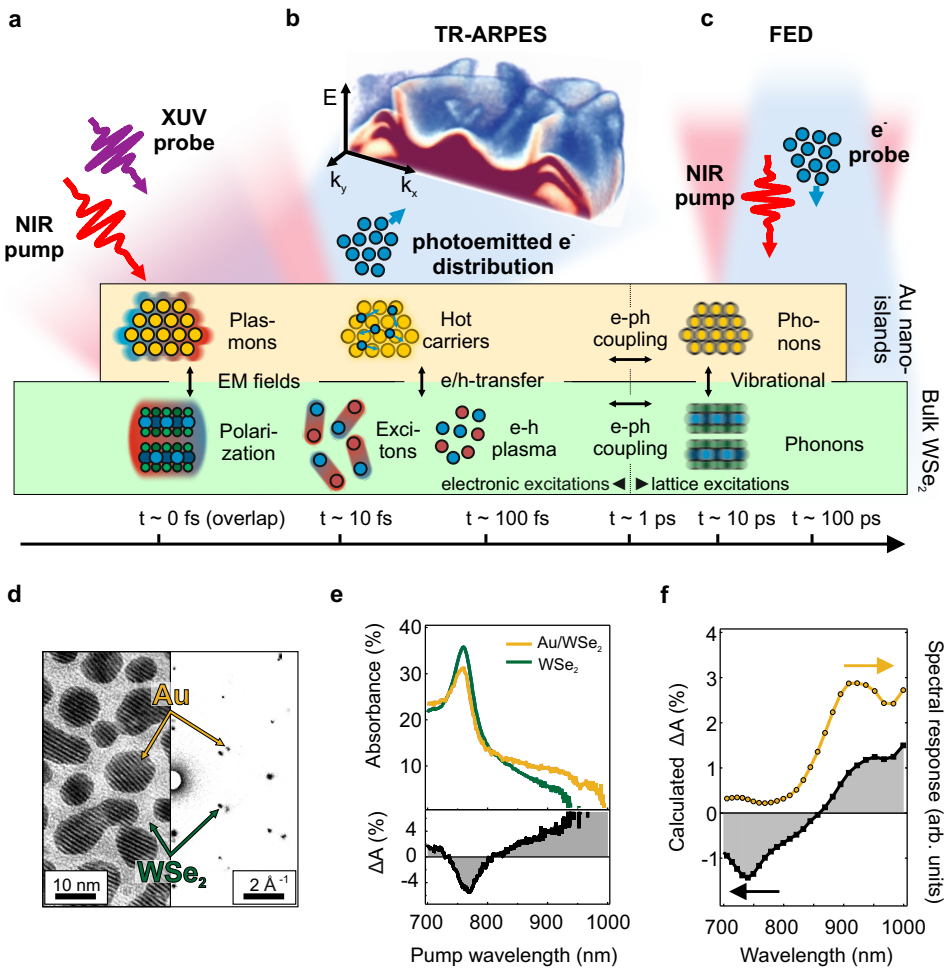

Figure 1: **Subsystem- and material-resolved study of ultrafast energy flow in a nanometal-semiconductor heterostructure. (a)** Schematic illustration of the techniques employed to probe different microscopic subsystems and their couplings in the heterostructure. Optical excitation by a pump pulse generates plasmons and hot carriers in the nanometal, and excitons in the semiconductor, probed by tr-ARPES (schematically represented in panel b). In both materials the lattice degrees of freedom (phonons) are excited by electron-phonon coupling, probed by FED (schematically represented in c and the right part of panel f). Interfacial interactions involve: electromagnetic fields (LSP and interfacial potentials), charge and energy transfer (Meitner-Auger, Föster or Dexter coupling) and vibrational coupling. **(b)** Cut-out (for $k_y > 0$) of the 3D ARPES signal $I(k_x,k_y,E)$ from the heterostructure surface with 21.7 eV XUV excitation. In a tr-ARPES experiment, one of such volumetric datasets is acquired for each pump-probe delay. **(c)** Scheme of a transmission FED experiment. **(d)** Electron microscopy (left) and diffraction (right) of epitaxial Au nanoislands (dark in the micrograph) on single-crystalline multilayer flakes of WSe_2 . In a FED experiment, performed in transmission geometry, one of such diffractograms is acquired for every pump-probe delay. **(e)** Upper panel: light absorption spectra of pure (green line) and Au-decorated WSe_2 (yellow line). Bottom panel: wavelength-dependent relative change of the absorption (δA) due to Au decoration. **(f)** Black squares: Calculated relative change of absorption using finite difference modelling (see Methods). Golden circles: spectral response of the electric field integral.

than peaked resonances [37]. In the following, we demonstrate that Au decoration tailors the pump electric field at the surface, producing a twofold effect: generation of localized surface plasmons (LSP) on the nanoislands, and strong field enhancement at the uncovered WSe_2 surface.

To gain insight on the optical response, we perform finite-element-method (FEM) calculations (see Methods and SI Sect. 3). We model the nanoparticles by vectorizing a part of the micrograph in Fig. 1 d, to reproduce a realistic arrangement of shapes. We obtain the far-

field absorbance variation due to the presence of Au decoration, which broadly matches the spectral distribution of the experimental result (black curves in Fig. 1 e and f). Discrepancies in amplitude and spectral distributions can be explained with the experimental uncertainty on the effective thickness of the individual sample, combined with the use of reference optical spectra and the limited size of the calculation (see Experimental Section). The FEM calculations enable estimating the contribution of plasmon-induced hot-carriers to the increased absorbance (yellow circles in Fig. 1 f, see Methods). The total absorbance variation (black curve) is adequately represented at photon energies smaller than the WSe_2 bandgap, thus confirming that, in this spectral range, photoabsorption in Au is dominated by plasmonic generation of injectable hot-carriers [38, 39, 40]. Since the nanoislands thickness is below the IMFP of hot carriers in Au [41] and the out-of-plane momentum matching constraints are relaxed due to strong vertical confinement, virtually all the plasmon-generated hot-carriers energetically above the Schottky barrier (SB) are available for injection.

For ultrashort light pulses, absorption also involves non-linear multiphoton processes. Close examination of the electric fields (see SI Sect. 2) shows a strong field enhancement of up to 30 times in the semiconductor near the nanoislands edges, which can induce multiphoton absorption. The amplitude and depth penetration of the field enhancement in WSe_2 increase as the photon energy becomes smaller than the A-exciton energy. In this spectral range, WSe_2 becomes more transparent and the plasmonic fields propagate further below the surface. Therefore, at high optical excitation intensities and long ($\geq$ 850 nm) wavelengths, we expect the photoabsorption in WSe_2 to occur predominantly by multiphoton processes.

From the volumetric ARPES data displayed in Fig. 1 b, we extract isoenergy maps of the momentum distribution. At the Fermi energy, the hexagonal *sp*-band and Shockley surface state form the Fermi surface of Au (111) (Fig. 2 a, top panel). At E-E_F=-0.8 eV (Fig. 2 a, bottom panel) we observe that the ARPES signal appears as the superposition of Au (111) and WSe_2 bandstructures, with the Au *sp*-band surrounded by the hexagonal arrangement of WSe_2 valence band maxima (VBM). By selecting a momentum direction ($\overline{\Gamma} - \overline{K}$ in the 2D Brillouin zone of WSe_2, black line in Fig. 2 a), we extract a momentum-energy map, and compare with ab-initio calculations (see SI Sect. 3) employing density functional theory (DFT) as overlaid on the data in Fig. 2 b. While the calculations have been performed for the two separate materials, the good agreement between DFT and experiment suggests a weak hybridization across the van der Waals gap (see SI Sect. 4).

The ARPES data combined with further core-level photoemission experiments reveal the details of band alignment (Fig. 2 c): considering the Schottky-Mott theory of contact potential, the Fermi level would be expected to be energetically near the valence band maximum. However, owing to the work function reduction observed in Au nanoparticles [42] and interfacial dipoles formation, the Fermi level is closer to the conduction band minimum of WSe_2, with Schottky barrier $\Phi_e = 0.470 \pm 0.005$ eV for electrons (ESB) and $\Phi_h = 1.000 \pm 0.005$ eV for holes (HSB) [43] (see SI Sect. 5). With this configuration, interfacial band bending is strongly suppressed, although a potential well of approximately 170 meV still exists, in the proximity of the nanoparticle interface.

2.1 Electron dynamics

To explore the charge dynamics during and right after the plasmonic excitation, we perform time-resolved ARPES experiments. Four observables, sketched in Fig. 2 d, allow us to distinguish the evolution of each material. In the semiconductor, we detect both the

occupied band position and the photoexcited population in the conduction band. The time resolution adds an additional dimension to the data and allows to capture transient population and scattering dynamics [27, 29]. In Au, we can track the dynamical evolution of the chemical potential, i.e. the energy position of the Fermi distribution center, and the electronic temperature. The main features involved in the dynamics are contained in a single momentum-energy cut (grey squares in Fig. 2 a).

In bare WSe_2 at room temperature, 800 nm pumping excites resonantly the A-exciton [29], thanks to the large bandwidth of 40 fs pulses. The excitons, observable as a transient population at the K-points (Fig. 2 e), scatter rapidly (18 ± 4 fs [27, 29]) to momentum-indirect states, with electrons populating the conduction band minimum (Σ valley) and holes occupying local valence band maxima (K or Γ points). The lifetime of indirect excitons is long owing to the suppressed radiative recombination probability arising from momentum mismatch [44, 45, 29]. We observe a bi-exponential population decay, with the shortest lifetime of 1.5 ± 0.1 ps (see SI Sect. 6) likely determined by hot exciton diffusion in the bulk and surface defect recombination [46]. In the heterostructure, 800 nm pumping at room temperature produces excited carriers in both Au and WSe_2 (Fig. 2 f, see also SI Fig. S4). To disentangle the contributions, we perform two measurements: one at room temperature, and another after cooling the heterostructure to 70 K (see also Fig. 3 e). The reduction of temperature in this system produces an increase of the WSe_2 bandgap (in optical measurements: $\approx$60 meV [47]), tuning the exciton resonance out of the pump bandwidth, which we will consider as the small detuning regime.

Fig. 3 a reports the electronic temperature (T_e) dynamics of Au obtained by fitting the data to Fermi-Dirac distributions (see SI Sect. 11). Compared to the well-known electron-lattice equilibration dynamics of bulk Au (see SI Sect. 12, shown in Fig. 3 a as a result of two-temperature model), the experimental T_e of the heterostructure rises on a longer timescale and to a lesser degree. This suggests efficient charge-transfer from the Au nanoislands to WSe_2, to such an extent that Au hot carriers are transferred before the non-equilibrium distribution can thermalize, a signature of strong exciton-plasmon interaction. The observation of plasmon-induced hot-carrier transfer is further supported by tracking the position of WSe_2 VBM and the chemical potential in the small detuning case (Fig. 3 b). The two features shift simultaneously in opposite directions, indicating that unbalanced amounts of charge are being transferred across the interface. These observations match optical measurements and FEM calculations, where we highlighted the relevance of LSP-induced injectable hot carriers in the absorption spectrum of the heterostructure (see SI Sect. 8 and 9).

The recovery dynamics in Fig. 3 b reveal the mechanisms immediately subsequent the charge-transfer process: an interfacial electrical field is generated, and the increase of the SB combines with hot-carrier relaxation to stop the hot-carrier injection. The injected carriers, after losing energy to the lattice of WSe_2, are rapidly back-injected to reach charge compensation, on a timescale of 250-300 fs. The charges re-injected in Au lose energy, producing the slow rise in electronic temperature observed in Fig. 3 a. A clear indication of the back-transfer process can be seen in Fig. 3 c, where the population dynamics of the Σ valley is displayed for the three cases of the bare WSe_2, and the heterostructure under resonant exitation and in the small detuning regime. The decay of the population becomes strikingly faster in the heterostructure with small detuning as back-injection offers a rapid channel for charge compensation. We find the decay time of the back-injected population to be 240 ± 30 fs by constrained multi-exponential fitting (see SI Sect. 7).

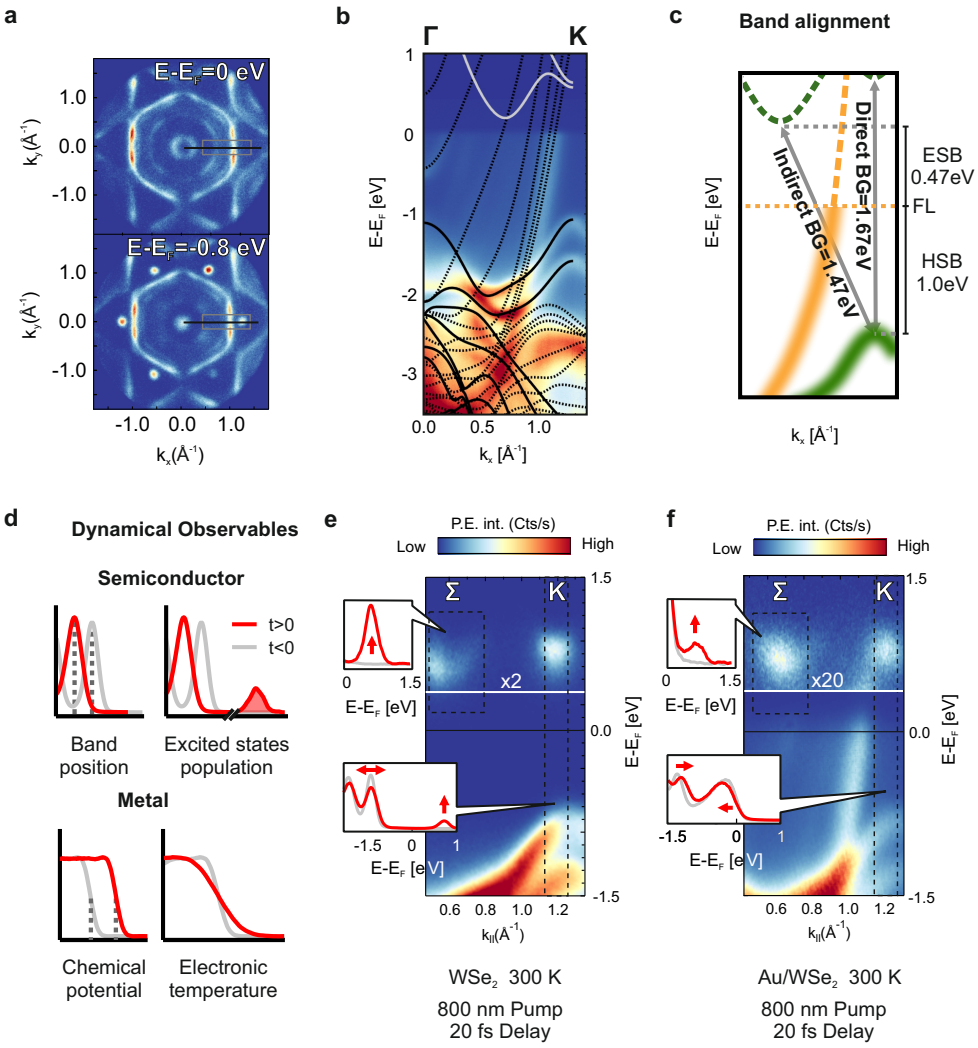

Figure 2: **Electronic structure of Au/WSe$_2$. (a)** Constant energy cuts of Au/WSe$_2$ in the first brillouin zone. Top panel: Fermi surface E-E$_F$=0 eV, with hexagonal sp-band and surface state (close to the Γ point), characteristic of the Au(111) facet. Bottom panel: isoenergy surface at E-E$_F$=-0.8 eV, showing the VBM at the K-points of WSe$_2$ (hexagonal array of dots). The black line (grey rectangle) shows the energy-momentum cut probed in panel b (panel f). **(b)** Γ-K momentum-energy cut of Au/WSe$_2$. The solid black and white curves show the valence and conduction bands of WSe$_2$ as derived by DFT. The dashed curves show the DFT-derived metallic states of Au. **(c)** Schematic picture of the band alignment: at the WSe$_2$ K points, the direct band gap (DBG) is 1.67 eV, larger than the indirect bandgap (IBG) at 1.47 eV. Due to nanostructuring, the Fermi Level (FL) position is closer to the conduction band than expected from the Schottky-Mott limit, with Electron and Hole Schottky Barriers (ESB and HSB) of 0.47 eV and 1 eV, respectively. **(d)** Schematic summarizing the observables employed to probe the dynamics of the heterostructure before (grey) and after (red) excitation. **(e)** Momentum-energy cut for the bare WSe$_2$ surface, acquired at +20 fs delay. The intensity above the white horizontal line (E-E$_F$=+300 meV) has been multiplied by 2. Both K and Σ valleys are populated. The insets show EDCs evolution within the dashed regions. **(f)** Same as (e), but for the Au/WSe$_2$ heterostructure, at +20 fs. The intensity above the white horizontal line (E-E$_F$=+300 meV) has been multiplied by 20.

In Fig. 3 c, the presence of a slow-decaying exciton population is evident at longer delays for the heterostructure. Its relative fraction changes from 70 ± 10 % to 30 ± 10 % when the excitation falls out of resonance with the A-exciton. This is the population of charge-neutral, thermalized excitons. They are formed by direct excitation with resonant pumping, and by plasmon-enhanced multiphoton absorption when the excitation is non-resonant. To support this interpretation, we measured the fluence dependence of the Σ-valley population at long

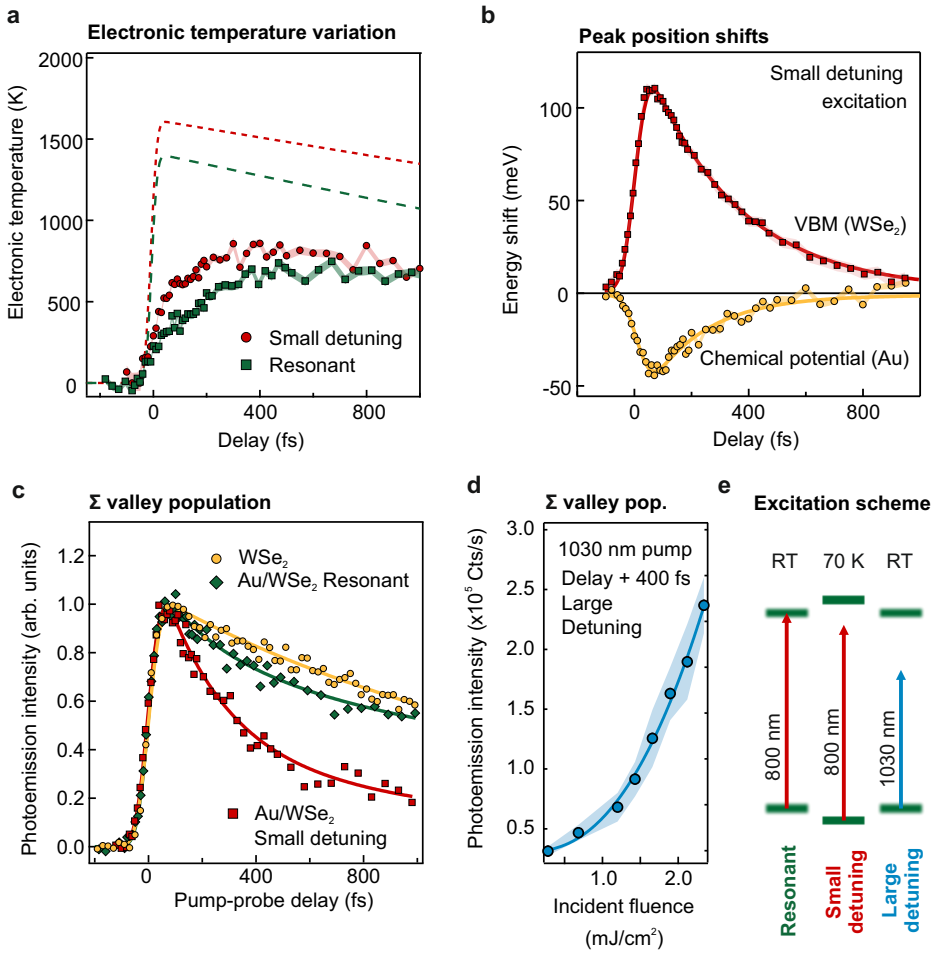

Figure 3: **Multi-observable electronic dynamics in Au/WSe_2.** **a** Electronic temperature as extracted from Fermi function fitting of the data, compared with 2TM prediction (dashed lines), using the experimental absorbed energy (from Fig. 1 e) and temperature-dependent experimental values of electron-phonon coupling constant, electronic and lattice heat capacities for nanostructured Au. **b** Dynamic shifting of Au Fermi edge (circles) and WSe_2 VBM (squares). Solid lines are fits of an exponential convolved with the instrument response function (IRF). The exponential decay characteristic times are 251 ± 24 fs (Au) and 318 ± 7 fs (WSe_2) respectively. **c** Population dynamics in the Σ valley for different experimental settings. For bare WSe_2, the solid line is an exponential fit convolved with the IRF, giving a decay time of 1.5 ± 0.08 ps. For the heterostructure, the solid lines are fits with double exponential decay convolved with the IRF. The second exponential is fixed at 1.5 ps, while the first is 240 ± 30 fs in both cases. The relative amplitude of the first decay changes from 36 ± 8 % to 72 ± 2 % when going from 300 K to 70 K. **d** Σ valley population at long delays vs fluence for 1030 nm photoexcitation. The solid line is a power law fit resulting in an exponent of 2.3 ± 0.3. Shaded areas show the experimental uncertainty discussed in the SI. **e** Schematic showing the excitation schemes employed. At room temperature, λ=800 nm is quasi-resonant with the first excitonic transition. At 70 K, the same wavelength is slightly out of resonance, in the small detunig regime. At room temperature, λ=1030 nm is strongly out of resonance, in the strong detuning regime that highlights plasmonic nonlinear effects.

(+400 fs) pump-probe delays in the strong detuning regime (1030 nm pumping at room temperature), reported in Fig. 3 d (blue circles). As demonstrated by the finite element calculations (see SI Sect. 2), long wavelengths and high fluences maximize multiphoton absorption in WSe_2. Fig. 3 e reports all the excitation schemes employed in the experiment. The population scales with fluence following a power law of exponent 2.3 ± 0.3, indicating a two-photon absorption process (see SI Sect. 7). The thermalized excitons give rise to a long-timescale dynamics as they diffuse towards the nanoparticles and recombine by transferring carriers to Au, discussed in the following.

2.2 Lattice dynamics

The vibrational response of the heterostructure is probed by FED [31]. Following optical excitation of the electrons, electron-phonon coupling increases the vibrational energy content, leading to the main quantity extracted with FED: the change of the atomic mean-squared-displacement (MSD) $\Delta\langle u^2\rangle$.

Fig. 4 a, shows the $\Delta\langle u^2\rangle$ of WSe_2 in the first 5 ps after photoexcitation for three sets of experiments: pure WSe_2 pumped in resonance with the A-exciton (λ=763 nm), Au-decorated WSe_2 (λ=763 nm), and Au-decorated WSe_2 with sub-band-gap (λ = 850 nm) excitation —all with similar excitation density (see Methods). The time-constants for lattice heating in response to resonant excitation drops from 1.73 ± 0.16 ps in pure WSe_2, to 1.19 ± 0.3 ps in Au-decorated WSe_2, and down to 0.68 ± 0.02 ps for sub-band-gap excitation. Pure WSe_2 does not show measurable lattice heating with 850 nm pumping (see SI Sect. 14). From the measurements of Fig. 4 a, it becomes obvious that Au-decoration accelerates carrier-lattice equilibration in WSe_2 and enables absorption of sub-band-gap photons, giving rise to even faster lattice dynamics.

The measurements of Fig. 4 a have been repeated for various fluences. The extracted time-constants (τ) and amplitudes of the fitted exponential decays are plotted as a function of the incident laser fluence in Fig. 4 b and Fig. 4 c, respectively. Pure WSe_2 has a time-constant of ≈1.6 ps at 7 mJ/cm^2 to ≈2 ps at 3 mJ/cm^2 (Fig. 4 b, blue data points). With Au decoration, the WSe_2 lattice response to the A-exciton becomes significantly faster and all measured time-constants cluster around 1.2 ps (Fig. 4 b, red data points). This is in clear agreement with the results of tr-ARPES experiments in Fig. 3 c. The accelerated lattice dynamics of WSe_2 results from charge-injection from Au, as the hot carriers reside only for short time in the semiconductor (Fig. 3 b). For pure WSe_2 pumped at the A-exciton resonance, the fluence dependence of the maximum MSD reached by carrier-lattice equilibration is close to linear (blue solid line, Fig. 4 c). When WSe_2 is covered by Au, the rise of the MSD is enhanced and it assumes a non-linear fluence dependence (Fig. 4 c).

Further acceleration of carrier-lattice relaxation is observed for sub-band-gap (850 nm) excitation (Fig. 4 b, orange data points). The time-constants are on the sub-picosecond timescale and as short as 500 fs at 1 mJ/cm^2. The non-linear fluence dependence of the maximum MSD can be represented with a power law of exponent 2.0±0.1. Thus, at the high fluences used in FED, which are all higher compared to the λ = 800 nm tr-ARPES experiment, absorption of sub-band-gap photons is dominated by two-photon absorption, in line with the observations in ARPES for the Σ valley population in Fig. 3 d.

Figure 4 d shows the lattice dynamics of Au and WSe_2 up to 200 ps after photoexcitation with sub-band-gap light. The MSD of Au is used to extract its lattice temperature evolution through the Debye-Waller factor. Both materials show a lattice response that can be approximated with multiexponential fitting. Regarding WSe_2, the MSD is first rising due to carrier-lattice relaxation with $\tau_1 = 0.74 \pm 0.02$ ps, followed by a decrease with $\tau_2 = 16 \pm 1$ ps, which we assign to phonon-phonon equilibration in WSe_2 [33].

In the 50-200 ps time interval, the atomic MSD of WSe_2 is again rising (by $5.3{\cdot}10^{-4}$Å^2, Fig. 4 d). The lattice dynamics of Au during the first 50 ps have bi-exponential behavior with $\tau_1 = 4 \pm 1$ ps, and $\tau_2 = 35 \pm 5$ ps. The fast, lattice-heating process is in the typical timescale (3-6 ps) for electron-phonon coupling in nano-Au, while the second is surprisingly slow for intrinsic carrier-lattice equilibration [48, 49]. The slow heating can arise from the transfer of lattice-equilibrated dark excitons [27] from WSe_2 towards Au and their dissociation to

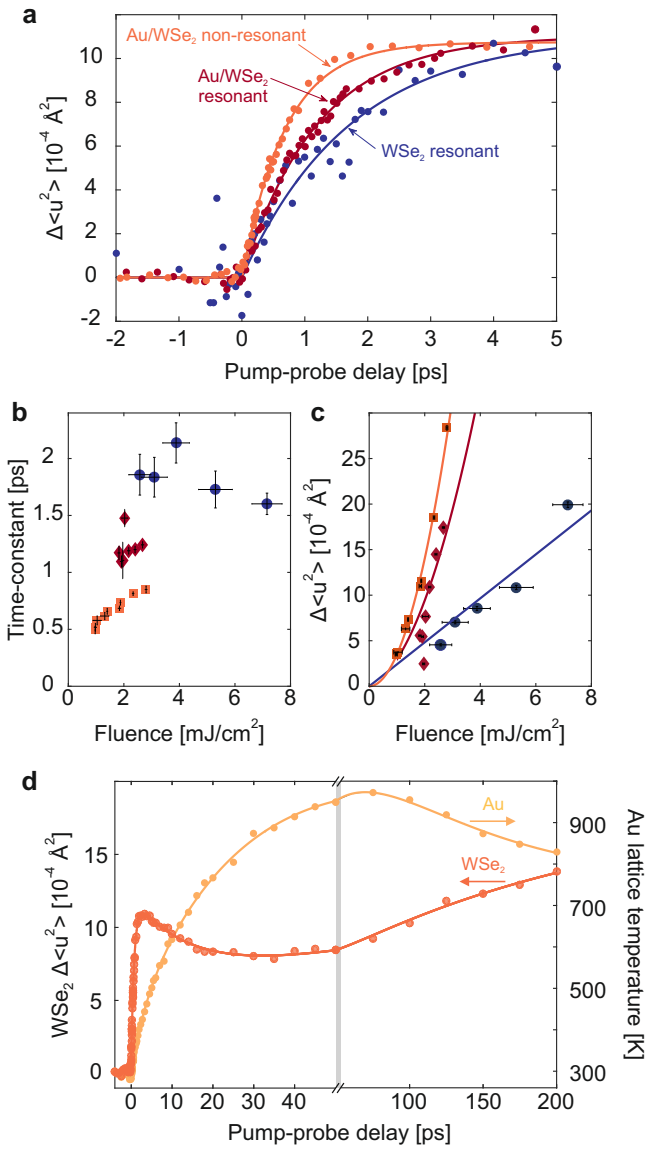

Figure 4: **Ultrafast lattice dynamics of Au/WSe_2 heterostructures.** **(a)** Enhancement of atomic MSD due to carrier-lattice coupling as a function of the pump-probe delay for resonant excitation of pure WSe_2, resonant excitation of Au/WSe_2, and non-resonant excitation of Au/WSe_2 shown with blue, red, and orange points, respectively. The corresponding solid lines are fits with exponential decay functions of the form: $A \cdot exp(-t/\tau)$, where τ is the time-constant and A is the maximum atomic MSD caused by carrier-lattice relaxation. **(b)** and **(c)** Time-constant for carrier-lattice coupling and maximum MSD after carrier-lattice equilibration, respectively (same color codes). **(d)** Long delay dynamics of the atomic MSD of WSe_2 (orange curve and left axis) and the corresponding lattice temperature evolution of Au (gold curve and right axis).

metallic *sp*-states [17]. Each of these events releases ≈1.5 eV (the indirect band gap of WSe_2) and generates hundreds of vibrational quanta. The maximum lattice temperature of Au is ≈ 970 K, while in the 50-200 ps time-interval it cools by 140 K (Fig. 4 d). The cooling of Au and the heating of WSe_2 at long time-delays is interpreted as re-equilibration of the two components by vibrational coupling, previously found in heterostructures of Au

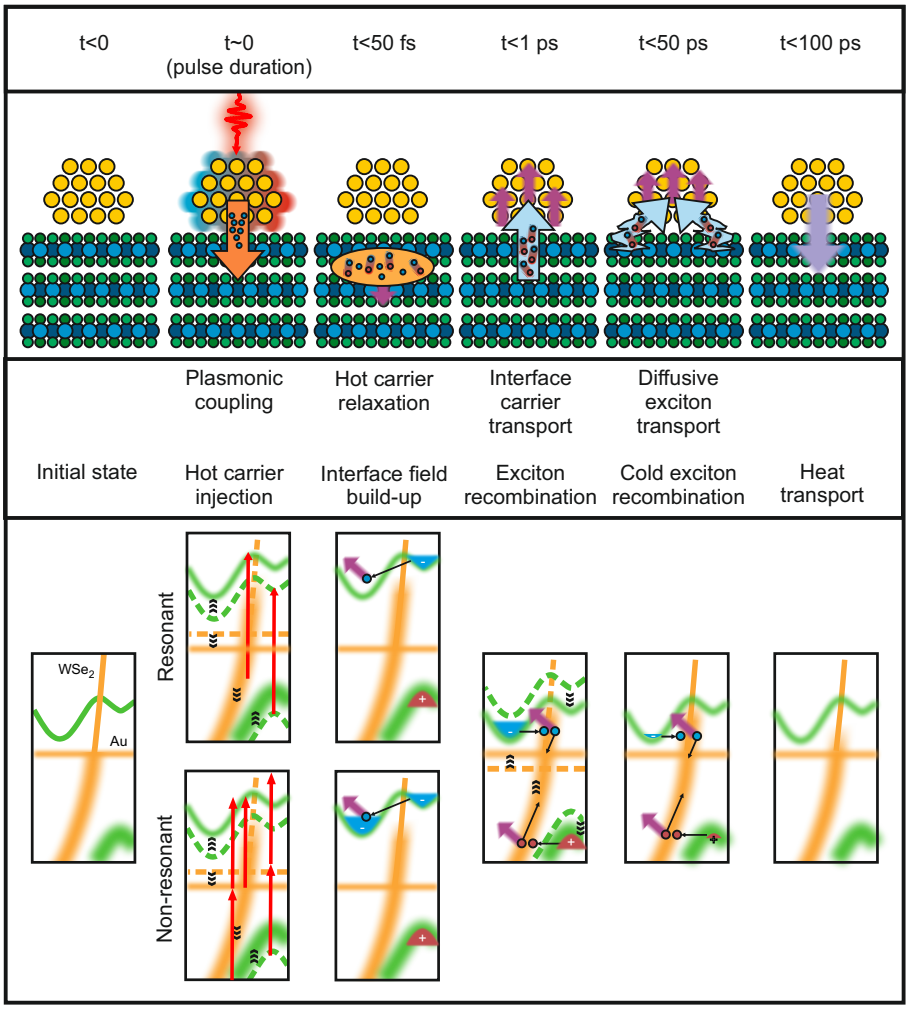

Figure 5: **Energy flow across the Au/WSe_2 heterostructure.** Schematic sequence of events and quasiparticle transfer unfolding in Au/WSe_2 heterostructure after NIR excitation. Top band shows a cartoon, real space picture. Solid orange arrows represent plasmon-induced hot-carrier transfer. Solid light blue arrows indicate hot exciton transfer. Wiggly light blue arrows represent diffusive exciton recombination via metallic Au states. Fuzzy purple arrows indicate hot phonon generation by electron-phonon coupling. The fuzzy lilac arrow shows the direction of vibrational energy transfer at long timescales. The bottom panel shows the correspnding electronic structure picture, with the two different cases of resonant and sub-bandgap pumping separated at short timescales. Red arrows indicate the relevant vertical optical transitions.

nanoclusters on various substrates [48, 49].

3 Discussion

Considering all experimental results, we can confirm the presence of a strong exciton-plasmon interaction, determine its microscopic origin, and assess the kinematics of the multi-directional energy flow across the interface. Figure 5 summarizes the observed processes in the Au/WSe_2 heterostructure in real-space (upper panels) and momentum-space (lower panels). In the interpretation of the data, it is important to notice that, while FED probes

the entire volume of the sample, tr-ARPES is extremely surface sensitive: for this reason we focus on observables that are homogeneous at the scale of a nanoparticle or a gap ($\approx$ 10 nm) at the timescales of interest ($>$ 10 fs), or we use the excitation wavelength to be intrinsically selective of the hot carriers while tracking population dynamics (see SI Sect. 10).

Optical illumination induces LSP at the nanoisland's surfaces and edges. In Au, plasmons produce highly energetic hot carriers scatter across the interface on extremely short timescales (<10s fs). Both electrons and holes are transferred, but the asymmetric SB produces an excess electron population. In the open WSe_2 gaps, the strong near-fields generate electrons and holes through non-linear multiphoton absorption: this gains relevance over hot-carrier injection or single-photon absorption at wavelengths $\geq$ 850 nm and fluences $\geq$ 1 mJ/cm^2.

After excitation, most of the injected hot carriers lose their energy in WSe_2 forming indirect (optically dark) excitons. Initially, when the carriers enter the semiconductor ballistically, they may undergo electronic scattering processes such as electron-hole collisions or surface/defect scattering. Although the strong excitonic binding energy in WSe_2 and the abrupt interfaces achievable in a meal/van-der-Waals interface suggest the significance of these mechanisms in damping the ballistic regime, dedicated experiments would be needed to ascertain their role. Subsequently, however, the hot carriers transfer energy to the lattice via electron-phonon scattering, which we detect at early times in the MSD dynamics of WSe_2.

Then, the hot unbalanced free electrons, confined by static and dynamic interfacial fields to the vicinity ($<$ 1nm) of the nanoisland, flow back to Au, re-equilibrating charge on a timescale of 240 $\pm$ 30 fs. The electronic temperature of Au raises only through carrier backflow on hundreds of femtoseconds timescales, in stark contrast with the classic model of plasmonics assuming thermalization of the metallic hot carriers before interfacial transfer.

In parallel, the hot carriers generated by non-linear multiphoton absorption, distributed in the crystal, turn into dark excitons by electron-phonon coupling with the lattice at subpicosecond timescales due to their large scattering phase-space. Both of these processes shorten the electron-lattice relaxation time of WSe_2 down to 500 fs for low fluence ($\leq$ 1 mJ/cm^2) and sub-bandgap ($\geq$ 850 nm) pumping. After electron-lattice relaxation in WSe_2 (t>1 ps), the remaining cold dark excitons move diffusively until they reach the nanoislands, where they dissociate and produce a second intense lattice-heating of Au on a timescale of 35 $\pm$ 5 ps. This process is maximized when using sub-bandgap pumping at high fluences, where nonlinear multiphoton effects generate large populations of dark excitons in the plasmonic hotspots appearing in a few tens of nanometers radius from the interface.

In conclusion, we have disentangled the contributions of individual materials and specific plasmonic, electronic and phononic excitations to interfacial energy transfer processes. We have demonstrated that strong plasmon-exciton interaction leads to immediate energy transfer to the semiconductor, with the nanometal being heated by carrier backflow and exciton recombination at two distinct timescales. The two-stepped energy backflow arises from the presence of two species of excitons: the ones generated by strong plasmon-exciton interaction in the vicinity of the nanoisland and the ones produced by non-linear absorption in the plasmonic hot-spots.

The Au/WSe_2 system is close to real-life applications, with the Au nanoislands offering plasmonic and catalytic properties and the WSe_2 displaying a rich excitonic structure that allows following different energy paths at different photon energies. The possibility of har-

vesting plasmonic energy into high energy excitons is a mechanism useful for optoelectronics and photochemistry [39], and the backflow arising from recombination might be minimzed by careful engineering of the band alignment and momentum-matching conditions. The subsequent energy flow causing intense, local, lattice heating of nanoscale Au is a quasi-thermal process that can be used for photothermal conversion and for catalyzing chemical reactions [50]. These findings offer new possibilities to tune the quasi-thermal response by controlling the exciton population, possibly with means other than multi-wavelength and fluence excitation protocol employed here. For example, interfacing Au nanoislands with more complex 2D semiconducting heterostructures [51] might allow electrical control of the exciton population and thus of photochemical performance. Even further, manipulating the valley degree of freedom might give access to band topology-controlled functionalities [20, 23].

4 Experimental Section

Time-resolved ARPES: The time-resolved ARPES experiments were performed using a home-built optical parametric chirped-pulse amplifier (OPCPA) with 500 kHz repetition rate [52]. The OPCPA is used to drive high-order harmonic generation (HHG) by tightly focusing laser pulses onto a Argon gas jet. The HHG produces a comb of odd harmonics of the driving laser, extending up to the 11th order. The co-propagating fundamental is separated from the XUV harmonic beam using reflection onto a silicon wafer at Brewster's angle. A single harmonic (7th order, 21.7 eV, p-polarized, pulse duration: 23±4 fs FWHM, energy width: 110 meV FWHM) is isolated by reflection off a focusing multilayer XUV mirror and transmission through a 400 nm thick Sn metallic filter. A photon flux of up to $2\text{x}10^{11}$ photons/s at the sample position is achieved [53]. The 800 nm pump was s-polarized, had pulse duration of 36±4 fs, incident fluence of 750 ±50μJ. The 1030 nm pump was s-polarized, had pulse duration of approx. 250 fs, and variable incident fluence. The bulk WSe_2 samples are handled by a 6-axis manipulator (SPECS GmbH). The data are acquired using a time-of-flight momentum microscope (METIS1000, SPECS GmbH) and processed using custom-built code [54] for Fig. 2 c, while all the dynamics was measured using a hemispherical electron spectrometer (PHOIBOS150, SPECS GmbH) to achieve higher statistical performance [55].

Femtosecond Electron Diffraction: The FED apparatus employs electron pulses to measure the ultrafast lattice dynamics in response to photoexcitation. The diameters of the probed and pumped (photoexcited) areas are 100 μm and 400 μm, respectively. For each diffraction peak, the intensity is extracted by direct integration of the total counts within a circle of 20 pixel diameter. The center of the circle coincides with the center of mass of the peak and it is recalculated for each diffraction pattern in order to eliminate the effect of instabilities of the electron gun and the magnetic lens. An ultrashort laser pulse (100 fs) of selected wavelength (TOPAS Prime NirUVis) excites the electronic subsystem. The lattice response is probed with a time-resolution in the order of 300 fs using ultrashort, high energy (60 keV) electrons pulses [31] that impinge on the thin, freestanding sample, producing a diffraction pattern in transmission (Fig.S9a). After the arrival of an ultrashort laser pulse, the intensity of all diffraction peaks (I_{hkl}) decreases, and the inelastic scattering background increases, due to the generation of phonons by excited charge carriers and the Debye-Waller effect.

The relative decay of the diffraction peaks is used to calculate the time-dependent change

of the atomic MSD ($\Delta\langle u^2\rangle$) through the formula:

$$\Delta\langle u^2\rangle = -\frac{3d_{hkl}^2}{4\pi^2}\ln\frac{I_{hkl}(t)}{I_{hkl}(t<0)}, \quad (1)$$

where d_{hkl} is the spacing between crystal planes for each diffraction peak. For each measurement the $\Delta\langle u^2\rangle$ is averaged over all the diffraction peaks. Thus, the present analysis does not explicitly take into account nonthermal lattice modes [56] and the distinct vibrational amplitudes for different types of atoms in compounds, since the aim is to compare the average MSD dynamics [33] for pure and Au-decorated WSe_2. For this purpose, the measurements of Fig.4 a have been performed adjusting the fluence in order to obtain the same maximum atomic MSD of $(10.99 \pm 0.09) \cdot 10^{-4}$Å^2. For pure WSe_2 the incident laser fluence is (5.3 ±0.6) mJ/cm^2, while for Au-decorated WSe_2 it is (2.18 ± 0.04) mJ/cm^2 for A-exciton pumping and (1.88 ± 0.02) mJ/cm^2 for sub-band-gap photoexcitation.

Sample preparation: Samples for ARPES were prepared by cleaving bulk WSe_2 crystals in vacuum (base pressure better than 5x10^{-11} mbar). The crystals were then cooled to 70 K, then Au was evaporated on the surface for 5 min at a calibrated rate of 2 ± 1Å/min. The deposition at low temperature ensures homogeneous coverage across the sample. The sample was then "annealed" at 300 K for 30 min to enable island formation before measurement. The average height of the nanoislands is calculated at 2 ± 1 nm by considering nominal film thickness (1 ± 0.5 nm) and average area coverage ($\approx 50\%$).

The multilayer free-standing membranes for the FED measurements were prepared by exfoliation from bulk single crystals (HQ Graphene). Large flakes of WSe_2 are first separated from the bulk single crystal with a lancet. Then the flakes are attached on a glass substrate with a water soluble glue (Crystalbond) and thinned down by exfoliation with a scotch tape. The thin areas of WSe_2 are then separated from the substrate with a scalpel and placed into water to separate WSe_2 from the glue. Finally, the floating flakes of WSe_2 are scooped out with a TEM copper grid held by a tweezer and left to dry. For the Au/WSe_2, the TEM copper grid with the flake has been placed in a UHV chamber and 2 nm of Au were evaporated on top with electron-beam-evaporation using a rotating sample holder for homogeneous deposition.

Optical measurements: Using optical microscopy we selected a spot on a thin flake of bare WSe_2 (∼20 nm) suspended over a TEM grid, choosing a flat (without wrinkles) part of the sample. For this point of the sample we have recorded the optical transmission and reflectance spectra (T and R, respectively) using a micro-absorbance spectrometer, a supercontinuum laser (FIANIUM) as the broadband light source, and a fiber spectrometer (Avantes). In all cases we have recorded dark and reference spectra. The absorption spectrum (A in %) was calculated as A=100-T-R. Subsequently, the flake has been decorated with 2 nm thick Au and the measurements have been repeated at the same spot on the sample.

Finite element calculations: To understand the distribution of fields at the surface and explore the linear response of the heterostructure, we simulated the optical response in the frequency domain using the Optics package in the commercial finite difference software COMSOL Multiphysics. A block of 100 nm x 200 nm x 500 nm was used to model the substrate, while 2 nm thick islands were extruded on the surface using a lateral profile extracted from a micrograph, to exactly match the effective spatial distribution. A 100

nm x 200 nm x 500 nm vacuum layer was added on top. The optical field was incident vertically with polarization along the x direction (maps in Fig. 1 are rotated 90°). The mesh was optimized to achieve minimum element quality (skeweness) >0.1. The cuboid is surrounded by periodic boundary conditions, except for the input and output planes (along the z direction), where perfectly matched layer conditions were used.

To evaluate the LSP-generated hot carrier photocurrent we integrate the expression:

$$P = \int_{V_{Au}} |E|^2 d\mathbf{r} \ , \tag{2}$$

over the nanoparticle volume. As discussed in [38], this is proportional to the number of LSP-generated hot-carriers crossing the interface in a Schottky junction. To calculate the local the field enhancement $|E|/|E0|$, we have simply evaluated the ratio between $|E|$, the modulus of the electric field in the heterostructure and $|E0|$ the modulus of the electrical field in absence of Au.

The presence of both hot-carrier dominated photoabsorption and field enhancement is robust against variations in the shape and thickness of the islands, including islands with Winterbottom shape that represents the equilibrium shape at high temperatures [57], as long as the average coverage of 50% with typical sizes of islands and gaps around 10 nm are preserved.

Statistical analysis: Time-of-flight generated multidimensional ARPES data have been preprocessed by binning the tabular data structure into 4-dimensional hypervolumetric data. During the binning procedure, image distortion correction, image registration, momentum, energy and pump-probe delay calibrations are applied according to the procedure described elsewhere [54]. Hemispherical analyzer ARPES data do not require binning. Calibration-based distortion correction, together with momentum, energy and pump-probe delay calibration have been applied in the preprocessing phase. The pump-probe time-traces were averaged over multiple scans of the delay stage. Data are presented using mean ± SD, i.e. 68% confidence intervals. The fitting procedures employed are based on the non-linear least square method. Data analysis is performed using custom built routines in the proprietary software IgorPro.

The raw diffraction patterns were corrected by dark image subtraction (electron beam off and same exposure time) and flat field correction (obtained with homogeneous illumination of the electron camera with a strongly defocused polycrystalline diffraction pattern). The intensity of each Bragg spot was integrated over a circular area, whose center matched the position of local maximum intensity. The pump-probe time-traces were averaged over multiple scans of the delay stage. The time-constants and amplitudes, extracted by nonlinear least squares fitting of exponential decay functions, have error bars representing the 68% confidence intervals. Data analysis is performed with custom built Matlab scripts.

Supporting Information

Supporting Information is available from the Wiley Online Library or from the author.

Acknowledgements

This work was funded by the Max Planck Society, the European Research Council (ERC) under the European Union's Horizon 2020 research and innovation and the H2020-EU.1.2.1. FET Open programs (Grant Numbers: ERC-2015-CoG-682843, ERC-2015-AdG-694097, and

OPTOlogic 899794), the Max Planck Society's Research Network BiGmax on Big-Data-Driven Materials-Science, and the German Research Foundation (DFG) within the Emmy Noether program (Grant Number: RE 3977/1), through SFB 951 "Hybrid Inorganic/Organic Systems for Opto-Electronics (HIOS)" (Project Number: 182087777, projects B12 and B17), the SFB/TRR 227 "Ultrafast Spin Dynamics" (projects A09 and B07), the Research Unit FOR 1700 "Atomic Wires" (project E5), and the Priority Program SPP 2244 (project 443366970). Tommaso Pincelli acknowledges financial support from the Alexander von Humboldt Foundation. Thomas Vasileiadis acknowledges support from the Marie Skłodowska-Curie widening fellowship (101003436 - PLASMMONS). Thomas Vasileiadis and Emerson Coy thank Prof. Stefan Jurga (NanoBioMedical Centre, AMU Poznań) for the use of the HR-TEM instrument. Emerson Coy Acknowledge the partial financial support from the National Science Centre (NCN) of Poland by the OPUS grant 2019/35/B/ST5/00248. Samuel Beaulieu acknowledges financial support from the NSERC-Banting Postdoctoral Fellowships Program. Niclas S. Mueller acknowledges support from the German National Academy of Sciences Leopoldina through the Leopoldina Postdoc Scholarship.

References

[1] M. Moskovits, *Nature Nanotechnology* **2015**, *10*, 1 6.

[2] M. L. Brongersma, N. J. Halas, P. Nordlander, *Nature Nanotechnology* **2015**, *10*, 1 25.

[3] S. Linic, S. Chavez, R. Elias, *Nature Materials* **2021**, *20*, 7 916.

[4] H. A. Atwater, A. Polman, *Nature Materials* **2010**, *9*, 3 205.

[5] C. Clavero, *Nature Photonics* **2014**, *8*, 2 95.

[6] A. Furube, S. Hashimoto, *NPG Asia Materials* **2017**, *9*, 12 e454.

[7] J. Langer, D. Jimenez de Aberasturi, J. Aizpurua, R. A. Alvarez-Puebla, B. Auguié, J. J. Baumberg, G. C. Bazan, S. E. J. Bell, A. Boisen, A. G. Brolo, J. Choo, D. Cialla-May, V. Deckert, L. Fabris, K. Faulds, F. J. García de Abajo, R. Goodacre, D. Graham, A. J. Haes, C. L. Haynes, C. Huck, T. Itoh, M. Käll, J. Kneipp, N. A. Kotov, H. Kuang, E. C. Le Ru, H. K. Lee, J.-F. Li, X. Y. Ling, S. A. Maier, T. Mayerhöfer, M. Moskovits, K. Murakoshi, J.-M. Nam, S. Nie, Y. Ozaki, I. Pastoriza-Santos, J. Perez-Juste, J. Popp, A. Pucci, S. Reich, B. Ren, G. C. Schatz, T. Shegai, S. Schlücker, L.-L. Tay, K. G. Thomas, Z.-Q. Tian, R. P. Van Duyne, T. Vo-Dinh, Y. Wang, K. A. Willets, C. Xu, H. Xu, Y. Xu, Y. S. Yamamoto, B. Zhao, L. M. Liz-Marzán, *ACS Nano* **2020**, *14*, 1 28, publisher: American Chemical Society.

[8] P. K. Jain, K. S. Lee, I. H. El-Sayed, M. A. El-Sayed, *The journal of physical chemistry B* **2006**, *110*, 14 7238.

[9] J. B. Khurgin, *Nature nanotechnology* **2015**, *10*, 1 2.

[10] C. Boerigter, R. Campana, M. Morabito, S. Linic, *Nature communications* **2016**, *7*, 1 1.

[11] G. V. Hartland, L. V. Besteiro, P. Johns, A. O. Govorov, *ACS Energy Letters* **2017**, *2*, 7 1641.

[12] S. Tan, A. Argondizzo, J. Ren, L. Liu, J. Zhao, H. Petek, *Nature Photonics* **2017**, *11*, 12 806.

[13] G. Tagliabue, J. S. DuChene, M. Abdellah, A. Habib, D. J. Gosztola, Y. Hattori, W.-H. Cheng, K. Zheng, S. E. Canton, R. Sundararaman, et al., *Nature Materials* **2020**, *19*, 12 1312.

[14] A. M. Brown, R. Sundararaman, P. Narang, A. M. Schwartzberg, W. A. Goddard III, H. A. Atwater, *Physical review letters* **2017**, *118*, 8 087401.

[15] M.-E. Kleemann, R. Chikkaraddy, E. M. Alexeev, D. Kos, C. Carnegie, W. Deacon, A. C. De Pury, C. Große, B. De Nijs, J. Mertens, et al., *Nature communications* **2017**, *8*, 1 1.

[16] X. Yan, H. Wei, *Nanoscale* **2020**, *12*, 17 9708.

[17] A. Grubišić Čabo, J. A. Miwa, S. S. Grønborg, J. M. Riley, J. C. Johannsen, C. Cacho, O. Alexander, R. T. Chapman, E. Springate, M. Grioni, J. V. Lauritsen, P. D. C. King, P. Hofmann, S. Ulstrup, *Nano Letters* **2015**, *15*, 9 5883, pMID: 26315566.

[18] J. Vogelsang, L. Wittenbecher, D. Pan, J. Sun, S. Mikaelsson, C. L. Arnold, A. L'Huillier, H. Xu, A. Mikkelsen, *ACS photonics* **2021**, *8*, 6 1607.

[19] C. Xu, H. W. Yong, J. He, R. Long, A. R. Cadore, I. Paradisanos, A. K. Ott, G. Soavi, S. Tongay, G. Cerullo, et al., *ACS nano* **2020**, *15*, 1 819.

[20] L. Li, L. Shao, X. Liu, A. Gao, H. Wang, B. Zheng, G. Hou, K. Shehzad, L. Yu, F. Miao, et al., *Nature nanotechnology* **2020**, *15*, 9 743.

[21] H. Shan, Y. Yu, X. Wang, Y. Luo, S. Zu, B. Du, T. Han, B. Li, Y. Li, J. Wu, F. Lin, K. Shi, B. K. Tay, Z. Liu, X. Zhu, Z. Fang, *Light: Science & Applications* **2019**, *8*, 1 9.

[22] J. R. Dunklin, A. H. Rose, H. Zhang, E. M. Miller, J. van de Lagemaat, *ACS Photonics* **2020**, *7*, 1 197.

[23] W.-H. Lin, P. C. Wu, H. Akbari, G. R. Rossman, N.-C. Yeh, H. A. Atwater, *Advanced Materials* **2022**, *34*, 3 2104863.

[24] M. Dendzik, A. Bruix, M. Michiardi, A. S. Ngankeu, M. Bianchi, J. A. Miwa, B. Hammer, P. Hofmann, C. E. Sanders, *Physical Review B* **2017**, *96*, 23 235440.

[25] N. F. Hinsche, A. S. Ngankeu, K. Guilloy, S. K. Mahatha, A. G. Čabo, M. Bianchi, M. Dendzik, C. E. Sanders, J. A. Miwa, H. Bana, et al., *Physical Review B* **2017**, *96*, 12 121402.

[26] A. Varas, P. García-González, J. Feist, F. García-Vidal, A. Rubio, *Nanophotonics* **2016**, *5*, 3 409.

[27] R. Bertoni, C. W. Nicholson, L. Waldecker, H. Hübener, C. Monney, U. De Giovannini, M. Puppin, M. Hoesch, E. Springate, R. T. Chapman, et al., *Physical review letters* **2016**, *117*, 27 277201.

[28] C. W. Nicholson, A. Lücke, W. G. Schmidt, M. Puppin, L. Rettig, R. Ernstorfer, M. Wolf, *Science* **2018**, *362*, 6416 821.

[29] S. Dong, M. Puppin, T. Pincelli, S. Beaulieu, D. Christiansen, H. Hübener, C. W. Nicholson, R. P. Xian, M. Dendzik, Y. Deng, et al., *Natural Sciences* **2021**, e10010.

[30] M. Sygletou, S. Benedetti, M. Ferrera, G. M. Pierantozzi, R. Cucini, G. Della Valle, P. Carrara, A. De Vita, A. di Bona, P. Torelli, et al., *Small* **2021**, 2100050.

[31] L. Waldecker, R. Bertoni, R. Ernstorfer, *Journal of Applied Physics* **2015**, *117*, 4 044903.

[32] L. Waldecker, T. A. Miller, M. Rudé, R. Bertoni, J. Osmond, V. Pruneri, R. E. Simpson, R. Ernstorfer, S. Wall, *Nature Materials* **2015**, *14*, 10 991.

[33] L. Waldecker, R. Bertoni, H. Hübener, T. Brumme, T. Vasileiadis, D. Zahn, A. Rubio, R. Ernstorfer, *Phys. Rev. Lett.* **2017**, *119* 036803.

[34] G. Nicolay, R. Claessen, F. Reinert, V. Strocov, S. Hüfner, H. Gao, U. Hartmann, E. Bucher, *Surface Science* **1999**, *432*, 1 95.

[35] A. C. Domask, K. A. Cooley, B. Kabius, M. Abraham, S. E. Mohney, *Crystal Growth & Design* **2018**, *18*, 6 3494.

[36] K. A. Cooley, R. Alsaadi, R. L. Gurunathan, A. C. Domask, L. Kerstetter, W. A. Saidi, S. E. Mohney, *Journal of Crystal Growth* **2019**, *505* 44.

[37] H. Sun, M. Yu, G. Wang, X. Sun, J. Lian, *The Journal of Physical Chemistry C* **2012**, *116*, 16 9000.

[38] B. Y. Zheng, H. Zhao, A. Manjavacas, M. McClain, P. Nordlander, N. J. Halas, *Nature communications* **2015**, *6*, 1 1.

[39] A. Manjavacas, J. G. Liu, V. Kulkarni, P. Nordlander, *ACS nano* **2014**, *8*, 8 7630.

[40] A. O. Govorov, H. Zhang, Y. K. Gun'ko, *The Journal of Physical Chemistry C* **2013**, *117*, 32 16616.

[41] A. M. Brown, R. Sundararaman, P. Narang, W. A. Goddard III, H. A. Atwater, *Acs Nano* **2016**, *10*, 1 957.

[42] Y. Zhang, O. Pluchery, L. Caillard, A.-F. Lamic-Humblot, S. Casale, Y. J. Chabal, M. Salmeron, *Nano letters* **2015**, *15*, 1 51.

[43] C. M. Smyth, R. Addou, S. McDonnell, C. L. Hinkle, R. M. Wallace, *2D Materials* **2017**, *4*, 2 025084.

[44] G. Wang, A. Chernikov, M. M. Glazov, T. F. Heinz, X. Marie, T. Amand, B. Urbaszek, *Reviews of Modern Physics* **2018**, *90*, 2 021001.

[45] M. Selig, G. Berghäuser, M. Richter, R. Bratschitsch, A. Knorr, E. Malic, *2D Materials* **2018**, *5*, 3 035017.

[46] M. Massicotte, P. Schmidt, F. Vialla, K. G. Schädler, A. Reserbat-Plantey, K. Watanabe, T. Taniguchi, K.-J. Tielrooij, F. H. Koppens, *Nature nanotechnology* **2016**, *11*, 1 42.

[47] A. Arora, M. Koperski, K. Nogajewski, J. Marcus, C. Faugeras, M. Potemski, *Nanoscale* **2015**, *7*, 23 10421.

[48] T. Vasileiadis, L. Waldecker, D. Foster, A. Da Silva, D. Zahn, R. Bertoni, R. E. Palmer, R. Ernstorfer, *ACS Nano* **2018**, *12*, 8 7710, pMID: 29995378.

[49] T. Vasileiadis, E. N. Skountzos, D. Foster, S. P. Coleman, D. Zahn, F. Krečinić, V. G. Mavrantzas, R. E. Palmer, R. Ernstorfer, *Nanoscale Horiz.* **2019**, *4* 1164.

[50] Y. Dubi, I. W. Un, Y. Sivan, *Chem. Sci.* **2020**, *11* 5017.

[51] C. Jin, E. Y. Ma, O. Karni, E. C. Regan, F. Wang, T. F. Heinz, *Nature nanotechnology* **2018**, *13*, 11 994.

[52] M. Puppin, Y. Deng, O. Prochnow, J. Ahrens, T. Binhammer, U. Morgner, M. Krenz, M. Wolf, R. Ernstorfer, *Optics express* **2015**, *23*, 2 1491.

[53] M. Puppin, Y. Deng, C. Nicholson, J. Feldl, N. Schröter, H. Vita, P. Kirchmann, C. Monney, L. Rettig, M. Wolf, et al., *Review of Scientific Instruments* **2019**, *90*, 2 023104.

[54] R. P. Xian, Y. Acremann, S. Y. Agustsson, M. Dendzik, K. Bühlmann, D. Curcio, D. Kutnyakhov, F. Pressacco, M. Heber, S. Dong, et al., *Scientific data* **2020**, *7*, 1 1.

[55] J. Maklar, S. Dong, S. Beaulieu, T. Pincelli, M. Dendzik, Y. W. Windsor, R. P. Xian, M. Wolf, R. Ernstorfer, L. Rettig, *Review of Scientific Instruments* **2020**, *91*, 12 123112.

[56] L. Waldecker, R. Bertoni, R. Ernstorfer, J. Vorberger, *Phys. Rev. X* **2016**, *6* 021003.

[57] K. Reidy, J. D. Thomsen, H. Y. Lee, V. Zarubin, Y. Yu, B. Wang, T. Pham, P. Periwal, F. M. Ross, *Nano Letters* **2022**, *22*, 14 5849.